INFALL SIGNATURES TOWARD DENSE CORES IN THE PERSEUS MOLECULAR CLOUD

J. L. Campbell[1,2], R. K. Friesen[2], P. G. Martin[3], P. Caselli[4], J. Kauffmann[5], and J. E. Pineda[4]

Draft version August 17, 2015, to be Submitted to The Astrophysical Journal

ABSTRACT

We report the results of an HCO^+(3–2) and N_2D^+(3–2) molecular line survey toward 91 dense cores in the Perseus molecular cloud using the James Clerk Maxwell Telescope, to identify the fraction of starless and protostellar cores with systematic radial motions. Most observed HCO^+ profiles are asymmetric, with protostellar cores more likely to exhibit line asymmetries than starless cores. We quantify the HCO^+ asymmetry using a dimensionless infall parameter, δ_v, and identify 20 cores with significant blue or red line asymmetry in optically-thick emission indicative of collapsing or expanding motions, respectively. We separately fit the HCO^+ profiles with an analytic infall model and determine physical infall (outflow) speeds toward 23 cores. Comparing the δ_v and analytic model results, we find that δ_v is a good tracer of core infall if the optically-thin emission is aligned with the model-derived systemic velocity. The infall speeds range from subsonic ($0.03\,\mathrm{km\,s^{-1}}$) to supersonic ($0.4\,\mathrm{km\,s^{-1}}$), where the supersonic infall speeds likely trace global rather than local (core) infall. Only 7/31 HCO^+-detected starless cores have spectra well-fit by the infall model, with half of these in clustered regions where global infall is more likely. Starless cores with masses greater than the Jeans mass ($M/M_J > 1$) are somewhat more likely to show infall motions. We find no trend of non-thermal line width with M/M_J, suggesting that any undetected infall motions are small and subsonic. Most starless cores in Perseus are either not in a state of collapse (or expansion) or in a very early stage of collapse.

Subject headings: ISM: individual (Perseus), ISM: jets and outflows, ISM: kinematics and dynamics, ISM: molecules, radio lines: ISM, stars: formation

1. INTRODUCTION

In nearby molecular clouds, stars of low mass like the Sun are found to form in dense cores (Myers 1985; Cernicharo 1991; Lada et al. 1993). The earliest stage of star formation consists of the gravitationally-driven collapse of a dense core (Larson 1969; Shu 1977), forming a protoplanetary disk and a young stellar object (YSO) which accretes surrounding material. The details of the collapse of starless dense cores to their protostellar counterparts remains an active area of research for which the observational study of collapsing dense cores is vital. These regions are predominantly studied with millimeter and sub-millimeter wavelengths, probing thermal continuum emission of dust grains (e.g., Enoch et al. 2006) and molecular line emissions of the gas component (e.g., Aikawa et al. 2003), respectively. Infrared observations are also used to characterize embedded protostellar objects (e.g., Jørgensen et al. 2007; Enoch et al. 2009; Evans et al. 2009). Observations of molecular transitions that trace high density gas ($n \gtrsim 10^4$ cm^{-3}) probe the physical and chemical composition of dense cores. In particular, the analysis of optically-thick molecular line emission is a useful tool for analysing the kinematics of core collapse

[1] Department of Astronomy and Astrophysics, University of Toronto, 50 St. George St., Toronto, Ontario, Canada, M5S 3H4; jessicalynn.campbell@mail.utoronto.ca
[2] Dunlap Institute for Astronomy and Astrophysics, University of Toronto, 50 St. George St., Toronto, Ontario, Canada, M5S 3H4
[3] Canadian Institute for Theoretical Astrophysics, University of Toronto, 60 St. George St., Toronto, Ontario, Canada, M5S 3H8
[4] Max-Planck-Institut für extraterrestrische Physik (MPE), Gießenbachstrasse 1, D-85741 Garching, Germany
[5] Max-Planck-Institut für Radioastronomie, Auf dem Hügel 6953121 Bonn, Germany

(Myers et al. 2000). Infall motions in centrally concentrated dense cores produce red-shifted self-absorption in optically-thick line profiles (Leung & Brown 1977), resulting in blue asymmetries that have become commonly used indicators of infall motion (see Leung & Brown 1977; Snell & Loren 1977; Mardones et al. 1997; Zhou 1992; Gregersen et al. 2000; Myers et al. 2000; Chira et al. 2014). Mardones et al. (1997) defined a dimensionless infall parameter to quantify these asymmetries,

$$\delta_v = \frac{V_{thick} - V_{thin}}{\Delta V_{thin}}, \qquad (1)$$

where blue asymmetries ($\delta_v < 0$) identify candidate dense cores undergoing collapse. Here V_{thick} is the line-of-sight velocity of the brightest component in the optically-thick line profile, V_{thin} is the line-of-sight velocity of the optically-thin line tracing the systemic velocity of the dense core, and ΔV_{thin} is the full width at half maximum (FWHM) of the optically-thin line.

Although infall motion results in blue asymmetries in optically-thick emission profiles, other systematic gas motions, such as rotation or molecular outflow, could in principle produce similar asymmetries (Snell et al. 1980; Adelson & Leung 1988; Narayanan et al. 2002). Studies of dense cores, however, indicate that rotation has an insignificant effect on core support (Bergin & Tafalla 2007, and references therein), suggesting that core infall and expansion or outflow should dominate over possible line asymmetry effects caused by rotation. Multiple cores along the line of sight can also complicate the observed line profiles, an effect that can be avoided by observing in optically-thin molecules to distinguish between the velocity structure of line profiles that are dominated by core kinematics and those resulting from a superposition of
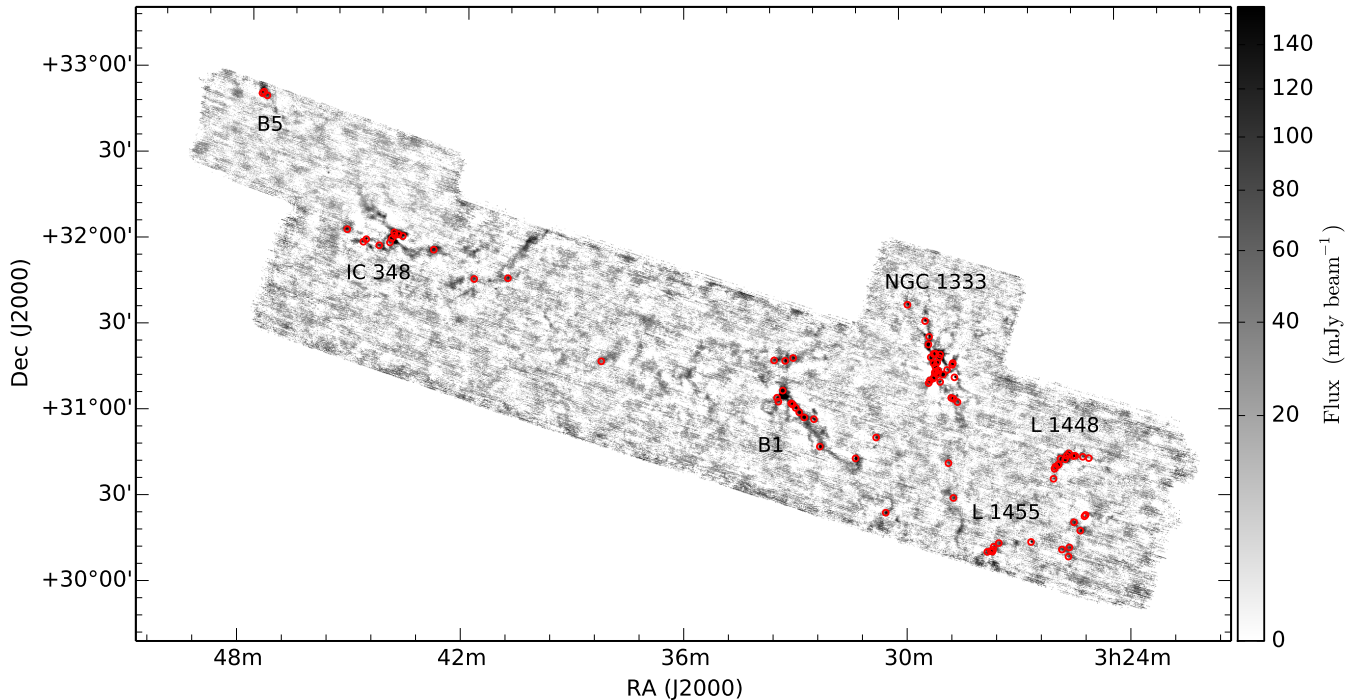
Figure 1. Targeted dense cores in our molecular line survey indicated by (red) circles (see Table 1), overlaid a 1.1-mm continuum map of the Perseus molecular cloud with $31''$ resolution taken with Bolocam on the CSO 10-m telescope, covering 7.5 deg^2 (143 pc^2 for a distance to Perseus of 250 pc) (Enoch et al. 2006). Six subregions of Perseus are indicated. Brightness scale is as square root.

cores (Mardones et al. 1997; De Vries & Myers 2005).

The Perseus molecular cloud (hereafter Perseus) is an example of a moderately clustered star forming region, more complicated than the quiescent, low mass Taurus molecular cloud, but less so than the turbulent Orion molecular cloud currently forming high-mass stars (Ladd et al. 1993, 1994; Kirk et al. 2007b). Perseus harbors several well-known clustered subregions and is an ideal environment for studying the formation of low-mass stars characterized by moderate levels of clustering and turbulence. Measurements of the distance to Perseus range from 220 to 315 pc, with several authors suggesting that Perseus might be composed of more than one cloud (e.g., Černis 1990; Cernicharo 1991; Cernis 1993; Luhman et al. 2003). Given the coherent velocity structure in Perseus and the similar distance estimates across the cloud (e.g., Schlafly et al. 2014), we will assume that Perseus is a single cloud at a distance of 250 pc.

In this paper we present the results of an $HCO^+(3–2)$ and $N_2D^+(3–2)$ survey performed using the James Clerk Maxwell Telescope (JCMT)[6] toward 91 dense cores in Perseus to identify cores with radial motions and to investigate the relationship between the infall (outflow) velocity and core stability. We discuss our source selection, observations, and data reduction in Section 2. The survey results follow in Section 3. We present our analysis in Section 4, including Gaussian line profile fitting, line asymmetry analysis using both the infall parameter, δ_v, and a modified infall parameter, δ_v^*, and using an analytic model. In Section 5, we explore how well δ_v traces infall using the results of the analytic model, discuss the observed infall speeds of Perseus cores, and quantify the

gravitational instability of cores using their Jeans mass, looking for a correlation with core infall velocity. A summary is given in Section 6.

2. OBSERVATIONS AND DATA REDUCTION

The observed Perseus cores were identified with 1.1-mm continuum data, selecting cores with an H_2 column density cutoff of $N(H_2) \geq 7 \times 10^{21}$ cm^{-2}, including both starless and protostellar cores. The dense cores surveyed span a significant extent of the projected cloud, as shown in the 1.1-mm Bolocam continuum emission map in Figure 1 (Enoch et al. 2006). Circles indicate the observed core positions, many of which are within clustered regions or groupings of the cloud. At the assumed distance of 250 pc to Perseus, the JCMT's HPBW at 230 GHz subtends 0.02 pc, roughly four times smaller than the typical size of dense cores in Perseus (Jijina et al. 1999; Kirk et al. 2006; Rosolowsky et al. 2008). Our molecular line observations are thus pencil-beam pointings through each dense core.

Our target list of 91 dense cores is summarized in Table 1, including the Right Ascension (RA) and Declination (Dec) pointing positions. We identified protostellar cores as those within $20''$ of protostellar sources in several catalogs as noted in the table (Enoch et al. 2006; Jørgensen et al. 2007; Enoch et al. 2009). We classified two more cores as protostellar based on the detection of associated outflows, despite their lacking infrared point-source detections (Chen et al. 2010; Schnee et al. 2012) (specified in notes to Table 1). Four cores were found to have more than one associated YSO (specified in notes to Table 1) and for these we reference the closest one. Our sample is divided roughly evenly into protostellar (49 %) and starless (51 %) cores.

Table 1
Summary of Observations

Source	RA (J2000)	Dec (J2000)	HCO+ T_{peak} (K)	rms (K)	N$_2$D+ T_{peak} (K)	rms (K)	Protostellar? (Y/N)	Reference ID[e]
(1)	(2)	(3)	(4)	(5)	(6)	(7)	(8)	(9)
D26	$3^h25^m00^s.3$	$30°44'10''.5$	$\cdots$	0.15	$\cdots$	0.21	N	$\cdots$
B16	$3^h25^m07^s.8$	$30°24'21''.6$	1.23	0.17	$\cdots$	0.84	N	Eb1
B15	$3^h25^m09^s.7$	$30°23'53''.0$	1.73	0.20	$\cdots$	0.15	N	Eb2
B31	$3^h25^m10^s.1$	$30°44'40''.9$	1.49	0.22	$\cdots$	0.24	N	Eb3
B11	$3^h25^m17^s.1$	$30°18'52''.9$	1.18	0.20	$\cdots$	0.14	N	Eb4
B30	$3^h25^m22^s.5$	$30°45'06''.6$	1.46	0.22	$\cdots$	0.17	Y	Ea22
S57[d]	$3^h25^m25^s.7$	$30°45'01''.7$	2.90	0.31	0.68	0.15	Y	C
B13	$3^h25^m26^s.9$	$30°21'52''.7$	$\cdots$	0.16	$\cdots$	0.22	N	Eb6
D38	$3^h25^m32^s.3$	$30°46'00''.3$	1.77	0.35	$\cdots$	0.16	N	$\cdots$
B6	$3^h25^m35^s.5$	$30°13'06''.2$	$\cdots$	0.18	$\cdots$	0.25	N	Eb7
B29[b]	$3^h25^m36^s.0$	$30°45'10''.8$	4.52	0.24	1.64	0.07	Y	Ea33
B1	$3^h25^m37^s.2$	$30°09'55''.3$	$\cdots$	0.19	$\cdots$	0.28	N	Eb9
B25[a,c]	$3^h25^m38^s.9$	$30°43'59''.7$	5.01	0.19	1.0	0.20	Y	Ea42
B27	$3^h25^m46^s.3$	$30°44'14''.0$	2.06	0.21	$\cdots$	0.16	Y	Eb11
B4	$3^h25^m47^s.5$	$30°12'26''.4$	$\cdots$	0.24	$\cdots$	0.24	N	Eb12
B24	$3^h25^m49^s.3$	$30°42'15''.2$	1.43	0.26	0.57	0.17	N	Eb13
B23	$3^h25^m50^s.6$	$30°42'01''.7$	1.68	0.28	0.69	0.16	N	Eb14
B22	$3^h25^m55^s.1$	$30°41'26''.2$	$\cdots$	0.16	$\cdots$	0.22	N	Eb15
B21	$3^h25^m56^s.4$	$30°40'42''.9$	$\cdots$	0.20	$\cdots$	0.28	N	Eb16
B20	$3^h25^m58^s.5$	$30°37'13''.5$	1.37	0.21	$\cdots$	0.20	N	Eb17
B10	$3^h26^m37^s.2$	$30°15'18''.9$	$\cdots$	0.29	$\cdots$	0.11	Y	Ea25
B8	$3^h27^m29^s.5$	$30°15'09''.1$	$\cdots$	0.32	$\cdots$	0.20	N	Eb20
B7[a]	$3^h27^m37^s.9$	$30°13'53''.2$	1.84	0.19	$\cdots$	0.14	Y	Ea48
B5	$3^h27^m39^s.0$	$30°12'53''.5$	4.08	0.25	$\cdots$	0.14	Y	Ea17
S50	$3^h27^m40^s.0$	$30°12'12''.8$	1.40	0.09	$\cdots$	0.21	N	$\cdots$
B2	$3^h27^m42^s.7$	$30°12'24''.5$	3.09	0.21	0.62	0.13	Y	Ea20
B3	$3^h27^m48^s.3$	$30°12'08''.2$	1.91	0.23	$\cdots$	0.13	Y	J8
B43	$3^h28^m32^s.4$	$31°04'43''.4$	1.51	0.10	$\cdots$	0.13	N	$\cdots$
B59	$3^h28^m36^s.7$	$31°13'23''.8$	4.54	0.29	$\cdots$	0.12	Y	Ea35
B45	$3^h28^m38^s.8$	$31°05'54''.2$	2.58	0.20	$\cdots$	0.21	Y	Ea4
S46	$3^h28^m39^s.1$	$31°18'24''.1$	1.80	0.23	$\cdots$	0.36	N	F123
S44	$3^h28^m40^s.1$	$31°17'48''.6$	1.87	0.27	$\cdots$	0.20	Y	J13
B19	$3^h28^m41^s.7$	$30°31°12''.3$	$\cdots$	0.16	$\cdots$	0.20	Y	Eb32
B46[b]	$3^h28^m42^s.5$	$31°06'13''.1$	1.82	0.29	0.60	0.11	N	F121
B64	$3^h28^m48^s.5$	$31°16'03''.0$	1.77	0.11	$\cdots$	0.14	N	$\cdots$
B26	$3^h28^m48^s.8$	$30°43'24''.5$	$\cdots$	0.98	$\cdots$	0.72	Y	Eb36
B60[a]	$3^h28^m55^s.3$	$31°14'27''.8$	3.99	0.20	$\cdots$	0.20	Y	Ea27
B80	$3^h28^m59^s.5$	$31°21'28''.7$	4.72	0.22	$\cdots$	0.26	Y	J17
B56	$3^h29^m00^s.2$	$31°11'52''.9$	2.89	0.22	$\cdots$	0.37	Y	Ea3
B72	$3^h29^m01^s.4$	$31°20'23''.1$	10.69	0.22	0.84	0.19	Y	Ea54
S39	$3^h29^m03^s.2$	$31°15'53''.7$	6.92	0.16	1.18	0.16	Y	Ea44
S38[a]	$3^h29^m03^s.7$	$31°14'47''.8$	5.66	0.29	$\cdots$	0.21	Y	Ea15
B71	$3^h29^m04^s.5$	$31°18'42''.7$	2.35	0.10	$\cdots$	0.15	N	$\cdots$
S37	$3^h29^m06^s.5$	$31°15'36''.3$	1.25	0.19	1.16	0.17	N	F110
S35	$3^h29^m07^s.4$	$31°21'48''.4$	3.35	0.23	$\cdots$	0.34	Y	Ea50
B65[d]	$3^h29^m07^s.8$	$31°17'18''.7$	2.06	0.10	$\cdots$	0.22	Y	S
S34	$3^h29^m08^s.8$	$31°15'12''.8$	4.19	0.16	1.27	0.19	N	F107
S33[a,b]	$3^h29^m09^s.9$	$31°13'31''.2$	6.41	0.08	0.88	0.14	Y	Ea12
S32	$3^h29^m10^s.2$	$31°21'42''.9$	6.27	0.21	$\cdots$	0.18	Y	Eb47 (IRAS)
B67[c]	$3^h29^m10^s.5$	$31°18'25''.0$	3.85	0.19	$\cdots$	0.19	Y	Ea21
S30[a]	$3^h29^m11^s.3$	$31°13'07''.5$	5.05	0.16	1.55	0.18	Y	Ea13
B74	$3^h29^m15^s.0$	$31°20'32''.1$	5.77	0.26	$\cdots$	0.30	N	$\cdots$
B55	$3^h29^m17^s.0$	$31°12'25''.8$	1.85	0.18	0.84	0.19	N	$\cdots$
B83[b]	$3^h29^m17^s.2$	$31°27'44''.4$	4.34	0.21	0.40	0.13	Y	Ea23
B82[a]	$3^h29^m18^s.4$	$31°25'02''.7$	3.59	0.27	0.80	0.18	Y	Eb53 (IRAS)
B54	$3^h29^m19^s.1$	$31°11'32''.1$	1.81	0.17	0.44[a]	0.19	N	$\cdots$
B85[b]	$3^h29^m23^s.4$	$31°33'15''.7$	2.63	0.22	0.69	0.14	Y	Ea19
B87	$3^h29^m52^s.0$	$31°39'03''.4$	4.91	0.27	$\cdots$	0.24	Y	Ea9
B17	$3^h30^m32^s.0$	$30°26'24''.0$	1.82	0.23	0.52	0.13	Y	Ea7
B34	$3^h30^m46^s.1$	$30°52'44''.0$	1.24	0.21	$\cdots$	0.36	Y	Eb63 (IRAS)
B28	$3^h31^m20^s.0$	$30°45'30''.5$	2.46	0.18	$\cdots$	0.22	Y	Ea5
B33	$3^h32^m18^s.0$	$30°49'45''.4$	3.10	0.20	1.18	0.18	Y	Ea2

Table 1
Summary of Observations

B36	$3^{\rm h}32^{\rm m}27^{\rm s}.4$	$30°59'22''.0$	$\cdots$	0.31	$\cdots$	0.16	N	Eb67
B37	$3^{\rm h}32^{\rm m}43^{\rm s}.2$	$31°00'00''.0$	0.92	0.22	$\cdots$	0.15	N	Eb70
B38	$3^{\rm h}32^{\rm m}51^{\rm s}.3$	$31°01'47''.9$	0.36	0.10	$\cdots$	0.19	N	Eb71
B40	$3^{\rm h}32^{\rm m}57^{\rm s}.0$	$31°03'21''.1$	0.57	0.15	$\cdots$	0.18	N	Eb72
B75	$3^{\rm h}33^{\rm m}00^{\rm s}.6$	$31°20'50''.0$	$\cdots$	0.20	$\cdots$	0.12	N	Eb73
B41	$3^{\rm h}33^{\rm m}02^{\rm s}.0$	$31°04'33''.5$	0.92	0.09	$\cdots$	0.14	N	Eb74
B42	$3^{\rm h}33^{\rm m}04^{\rm s}.3$	$31°04'57''.5$	1.23	0.16	$\cdots$	0.20	N	Eb75
B73	$3^{\rm h}33^{\rm m}13^{\rm s}.8$	$31°19'51''.3$	$\cdots$	0.22	$\cdots$	0.35	Y	Ea39
B52[b]	$3^{\rm h}33^{\rm m}17^{\rm s}.9$	$31°09'27''.8$	6.93	0.22	1.22	0.12	Y	Ea29
B44	$3^{\rm h}33^{\rm m}25^{\rm s}.2$	$31°05'35''.4$	0.52	0.11	$\cdots$	0.16	N	Eb82
B48	$3^{\rm h}33^{\rm m}27^{\rm s}.3$	$31°06'58''.7$	2.45	0.22	$\cdots$	0.19	Y	Ea30
B77	$3^{\rm h}33^{\rm m}31^{\rm s}.8$	$31°20'01''.9$	0.85	0.19	$\cdots$	0.21	N	Eb85
BS10	$3^{\rm h}38^{\rm m}15^{\rm s}.1$	$31°19'44''.7$	$\cdots$	0.36	$\cdots$	0.37	N	$\cdots$
B91	$3^{\rm h}40^{\rm m}49^{\rm s}.7$	$31°48'34''.2$	$\cdots$	0.27	$\cdots$	0.20	Y	Eb89
B92	$3^{\rm h}41^{\rm m}45^{\rm s}.2$	$31°48'08''.7$	$\cdots$	0.73	$\cdots$	$\cdots$	N	Eb93
B95	$3^{\rm h}42^{\rm m}52^{\rm s}.5$	$31°58'11''.6$	$\cdots$	0.19	$\cdots$	0.20	Y	Eb97
S13[a]	$3^{\rm h}43^{\rm m}44^{\rm s}.0$	$32°02'46''.6$	2.09	0.27	$\cdots$	0.35	N	F27
B112[c]	$3^{\rm h}43^{\rm m}51^{\rm s}.1$	$32°03'21''.1$	4.25	0.27	0.77	0.13	Y	Ea16
B113[b]	$3^{\rm h}43^{\rm m}57^{\rm s}.2$	$32°03'01''.6$	6.56	0.51	0.53	0.16	Y	Ea11
B115	$3^{\rm h}43^{\rm m}58^{\rm s}.2$	$32°04'01''.3$	2.70	0.21	$\cdots$	0.16	N	F23
B106	$3^{\rm h}44^{\rm m}01^{\rm s}.8$	$32°01'54''.6$	6.18	0.35	0.75	0.15	Y	Ea32
B102	$3^{\rm h}44^{\rm m}05^{\rm s}.1$	$32°00'27''.8$	0.76	0.11	$\cdots$	0.15	N	$\cdots$
B100	$3^{\rm h}44^{\rm m}22^{\rm s}.6$	$31°59'23''.7$	1.54	0.10	$\cdots$	0.16	N	$\cdots$
B104[c]	$3^{\rm h}44^{\rm m}44^{\rm s}.2$	$32°01'26''.9$	4.24	0.21	$\cdots$	0.34	Y	Ea8
B103	$3^{\rm h}44^{\rm m}48^{\rm s}.9$	$32°00'31''.8$	1.76	0.20	$\cdots$	0.14	N	F15
B116	$3^{\rm h}45^{\rm m}15^{\rm s}.9$	$32°04'48''.7$	1.74	0.11	$\cdots$	0.14	N	$\cdots$
B121	$3^{\rm h}47^{\rm m}33^{\rm s}.5$	$32°50'55''.1$	$\cdots$	0.18	$\cdots$	0.19	N	Eb121
S2	$3^{\rm h}47^{\rm m}39^{\rm s}.0$	$32°52'11''.2$	1.25	0.20	$\cdots$	0.25	N	F6
S1	$3^{\rm h}47^{\rm m}41^{\rm s}.8$	$32°51'40''.3$	4.39	0.18	$\cdots$	0.29	Y	Ea53

[a] More than one dense core along the line of sight (Section 2).
[b] Systemic velocity sufficiently aligned with brightest HCO$^+$ peak (Section 4.1).
[c] More than one nearby ($< 20''$) YSO (Section 2).
[d] Classified as protostellar based on the detection of associated outflows, despite lacking infrared point-source detections.
[e] Letters of the YSO reference ID designating their catalog source – J for Jørgensen et al. (2007), Ea for Enoch et al. (2009), Eb for Enoch et al. (2006), F for Friesen et al. (2013), C for Chen et al. (2010), S for Schnee et al. (2012) – and associated source number in that catalog.

Pointed observations of these dense cores in Perseus were performed using JCMT. Targets were observed in the HCO$^+$(3–2) and N$_2$D$^+$(3–2) rotational transitions in position-switching mode, with assumed rest frequencies of 267.557619 GHz and 231.321665 GHz, respectively. Observations were taken with an 1800 MHz bandwidth using the A3 front-end receiver and ACSIS back-end, operating with a half-power beam width (HPBW) of $19''.7$. The spectral resolution was 30.5 kHz, corresponding to a velocity resolution of 0.03 km s^{-1} for the HCO$^+$(3–2) emission line and 0.04 km s^{-1} for the N$_2$D$^+$(3–2) emission line. Observations were conducted between September 2007 and September 2009.

The reduced data were downloaded from the JCMT CADC archive. A discrepancy was discovered between the velocity axis of the archival data, calculated using the rest frequency in the data headers following the radio definition, and the known line-of-sight local standard of rest velocities ($V_{\rm LSR}$) of the observed cores. This was rectified by converting between frequency and velocity using the center frequency keyword in the header rather than the rest frequency, producing spectra that agree with the known core $V_{\rm LSR}$ values. The center frequencies for HCO$^+$(3–2) and N$_2$D$^+$(3–2) used were 267.55192 GHz and 231.31671 GHz, respectively. As a check, we downloaded the raw data for several targets from the archive and re-reduced these using the Starlink software. We found that the calculated velocity axis agreed with our correction to the calibrated archive data and consequently it also agreed with the known core $V_{\rm LSR}$ values. All spectra were calibrated from antenna temperature (T_A^*) to main-beam temperature ($T_{\rm MB}$) using a main-beam efficiency of $\eta_{\rm MB} = 0.69$.

Targets with multiple repeats were co-added by taking their weighted average, where each spectrum was weighted by the inverse square of the baseline rms. Spectra were then smoothed by convolving with a Hanning window of size three and decimated manually, effectively reducing the velocity resolution from 0.03 km s^{-1} to 0.1 km s^{-1} for HCO$^+$(3–2) and from 0.04 km s^{-1} to 0.1 km s^{-1} for N$_2$D$^+$(3–2). This velocity resolution ensures that three independent velocity channels span the narrowest optically-thin line profile. As listed in Table 1, the resulting baseline rms for HCO$^+$ ranged from 0.08 K to 0.98 K, and for N$_2$D$^+$ from 0.07 K to 0.84 K.

All spectral line fitting was performed using the Python Scipy `curve_fit` routine.[7] Linear baselines were fit to each spectrum near emission lines for baseline subtraction. A linear correction to the baseline was insufficient for one target (B60) and so a third degree polynomial was used. We fit a linear combination of Gaussian components to the emission lines to measure the

[7] http://www.scipy.org/

Table 2
Summary of Perseus Dense Core Detection, Infall, Outflow, and Stability Statistics

	Detected	Multiple Components	Single[a] Gaussian Fit	Infall[a]	Outflow[a]	$M/M_J > 1$[b]
Starless	33/46	2	14/31	7/31	1/31	7/30
Protostellar	39/45	12	4/27	7/27	8/27	16/27

Note. — The percentages of sources well-fit by a single Gaussian and those that show infall and outflow motions do not sum to 100. Some cores have asymmetric HCO$^+$ line profiles, but the resulting uncertainty on V_{in} from the HILL5 model was larger than the returned V_{in} magnitude, and was thus not included in our infall/outflow analysis.

[a] Numbers are calculated from the number of detected sources in each category, removing the sources with multiple components along the line of sight.

[b] Numbers are calculated from the number of detected sources in each category with continuum data, removing the sources with multiple components along the line of sight. Note that one 'static' starless core did not have continuum data.
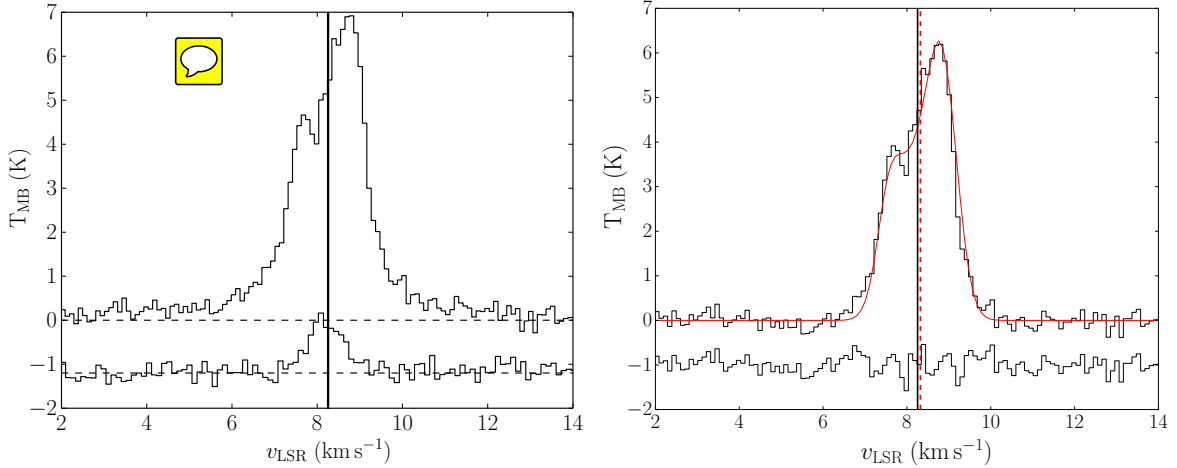
Figure 2. Left: Optically-thick HCO$^+$ (top) and optically-thin N$_2$D$^+$ (bottom, offset from zero) detections for source S39 as representative examples of the molecular line survey. This particular source exhibits a strong red asymmetry, with its measured systemic velocity, V_{thin} (solid vertical line), found in close proximity to the absorption dip and the line profile center. Right: The HCO$^+$ outflow profile (top) after removal of a broad Gaussian (see text) over-plotted by the best fit of the analytic model (red), with the resulting residuals shown below (offset from zero) for source S39. The observed systemic velocity (V_{thin}) and the modeled value (V_{mod}) are shown in solid black and dashed red vertical lines, respectively.

source velocity, amplitude, and velocity dispersion. For detected HCO$^+$ and N$_2$D$^+$ emission that only required a single Gaussian to be fit, we list the amplitude of the fit as T_{peak} in Table 1. For detected HCO$^+$ emission that required more than one Gaussian to be fit, we list the maximum amplitude of the data as T_{peak} in Table 1. The systemic velocity (V_{thin}) and the velocity dispersion (σ_{thin}) of N$_2$D$^+$ are listed in Table 3. Further details of the Gaussian line profile fitting is discussed in Section 4.1.

3. RESULTS

In the Appendix all HCO$^+$ line profiles are shown in Figure A.1 and all N$_2$D$^+$ line profiles are shown in Figure A.2, with sources in order of increasing RA as in Table 1.

We set a signal-to-noise ratio (S/N) threshold of 3 in T_{MB} using the (brightest) Gaussian fit amplitude for a source detection. Of the 91 observed sources, 72 (79 %) yield detections in HCO$^+$. Protostellar sources were more likely to be detected (39/45) than starless (33/46). The observed HCO$^+$ line profiles varied from symmetric and of approximately Gaussian shape to very complex, with two sources (B80, S57) having line profiles too com-

plex for the analysis in this paper. We detect 23 (25 %) of the dense cores in N$_2$D$^+$, all of which were detected in their HCO$^+$ counterparts. We additionally include source B54; it exhibits an N$_2$D$^+$ detection with S/N of only 2.3 but the profile is well aligned with the line profile of its HCO$^+$ counterpart. Table 2 summarizes the statistics of the detection results.

We show a representative optically-thick HCO$^+$ profile with its corresponding optically-thin N$_2$D$^+$ profile in Figure 2 (left), with the latter shifted downward to show the full extent of the velocity structure in both molecules.

4. ANALYSIS

In this section we outline details of the Gaussian fitting procedure performed on all emission line profiles (Section 4.1), how line asymmetries in HCO$^+$ profiles are quantified (Section 4.2.1), and the HILL5 model used to obtain physical parameters of the dense cores (Section 4.2.2).

To ensure that the observed HCO$^+$ line profiles are dominated by internal core kinematics, we first identify cores where optically-thin line tracers reveal multiple velocity components that are likely due to secondary

sources along the line of sight. We do not detect any secondary cores in the N_2D^+ emission profiles. Through N_2H^+ (Kirk et al. 2007b) and NH_3 (Rosolowsky et al. 2008) surveys, we identify eight cores with multiple components. Of these, seven are protostellar. These sources are specified in Table 1 and were omitted in further analysis.

There remained seven sources that exhibit line asymmetries in the optically-thick HCO^+ emission, but where examination by eye revealed that the observed systemic velocity was closely aligned with the brightest HCO^+ peak (discussed in Section 4.2.1 and noted in Table 1). For a spherically symmetric core undergoing bulk radial motion, the systemic velocity should trace the line profile center (De Vries & Myers 2005). It is therefore likely that the observed line profiles are due to multiple cores along the line of sight rather than internal core kinematics. All seven of these sources are found to be protostellar. The secondary sources might still be in their early stages of core evolution such that the dense gas tracers have not attained a significant enough abundance to be detectable at our sensitivity or in the above-mentioned N_2D^+ and NH_3 surveys used in this paper. Another possibility is that the velocity structure seen in HCO^+ is due to lower density gas emitting in filamentary regions surrounding the core, with the dense core moving relative to the surrounding gas. We also remove these sources from further analysis.

4.1. Gaussian Line Profile Fitting

To quantify asymmetries observed in the HCO^+ line profiles we perform Gaussian line profile fitting for the calculation of the infall parameter (δ_v) defined in Equation 1. The HCO^+ profiles often showed complex velocity structure and so were fit with a combination of Gaussians. An F-test was used to determine the most appropriate fit, with a false-rejection probability of 0.05 corresponding to a confidence level of 95 %.

To be fit accurately most HCO^+ profiles required only one or two Gaussian components, with some requiring a third Gaussian to fit broad, high velocity line wings likely from YSO-driven molecular outflows. One source, S33, was unique in that a fourth Gaussian component was required to fit an additional feature.

N_2D^+ contains hyperfine structure (e.g., Gerin et al. 2001) but this is not observable given our velocity resolution and low S/N. All of these spectra were thus fit with a single Gaussian. The statistics from the Gaussian profile fitting results are summarized in Table 2.

4.2. Infall Analysis

4.2.1. Line Asymmetry

For a spherically symmetric and static core observed in an optically-thick molecule, a self-absorption dip appears at the systemic velocity of the core where the gas density and excitation temperature peak, around which the emission line profile is symmetric (De Vries & Myers 2005). As the core undergoes collapse, the gas being redshifted becomes self-absorbed by gas with a lower excitation temperature, yielding the classic blue-asymmetric infall profile (Leung & Brown 1977; De Vries & Myers 2005). If, however, the core is undergoing outward radial motion, the gas being blueshifted will be locally self-

absorbed and the emission line profile will be red asymmetric.

To characterize dense cores that are likely to be collapsing and actively forming stars, we quantify the line asymmetries present in HCO^+ profiles using a dimensionless infall parameter, δ_v (see Equation 1). This method is independent of any physical model, is best suited to optically-thick profiles with two well-defined peaks, and is ambiguous for double-peaked profiles with equal intensities (Mardones et al. 1997). Furthermore, De Vries & Myers (2005) find that cores with comparatively high velocities begin to flatten out on either the red or blue side of HCO^+ emission for infall and outflow kinematics, respectively, resulting in a "shoulder" profile without two distinct peaks. To focus on the most asymmetric profiles that are the most likely to be representative of self-absorption caused by radial kinematics, we first quantify temperature asymmetries in the two brightest velocity components in optically-thick HCO^+ emission profiles in T_{MB}. This is done by measuring the ratio of the blue-red temperature difference of the two main velocity components to the error in that difference,

$$\delta_T = \frac{T_{\mathrm{blue}} - T_{\mathrm{red}}}{\sqrt{\sigma_{T_{\mathrm{blue}}}^2 + \sigma_{T_{\mathrm{red}}}^2}}, \qquad (2)$$

a parameter that has been used on its own to trace infall (e.g., Myers et al. 1995; Emprechtinger et al. 2009). We use the uncertainty from our Gaussian fitting procedure as our error measurement rather than the rms noise (Mardones et al. 1997) and restrict our analysis to those sources characterized by $|\delta_T| > 2$.

Neglecting sources with more than one known or suspected dense core along the line of sight, we find 20 cores with significant temperature asymmetries in their HCO^+ line profiles. These sources are listed in Table 3. Note that Table 3 also includes a different subset of sources where the line profiles could be fit by an analytic infall model, described below. The sources where δ_v is well-constrained have entries in Column 11. The running source name is indicated in Column 1. Optically-thin measurements are listed in Columns 2 and 3, where V_{thin} is the systemic velocity of the core and σ_{thin} is the velocity dispersion. For sources not detected in N_2D^+, we obtain optically-thin measurements of V_{thin} and σ_{thin} from N_2H^+ (Kirk et al. 2007b) and NH_3 (Rosolowsky et al. 2008) line surveys; for such sources we list the reference ID in Column 4. The δ_v measurements for these sources are shown in Column 11. A higher fraction of these cores with strong temperature asymmetries in their HCO^+ profiles was found to be protostellar (55 %) compared to those that do not exhibit line asymmetries (36 %). Given that our source selection is approximately equally divided into protostellar (49 %) and starless (51 %) cores, we conclude that protostellar cores are more likely to exhibit line asymmetries than are starless cores.

4.2.2. Analytic HILL5 Modeling

Since the δ_v analysis does not provide physical infall velocities of the cores, we fit the observed HCO^+ line profiles using a one-dimensional analytic model of a collapsing core (De Vries & Myers 2005). We use the HILL5 model, which assumes that the excitation temperature follows a linear relationship with optical depth along the

Table 3
Summary of Perseus Dense Core Kinematics

	$N_2D^+/N_2H^+/NH_3$ Gaussian Fit Results			HCO^+ HILL5 Fit Results						Asymmetry Analysis	
Source	$V_{\rm thin}$ $(\rm km\,s^{-1})$	$\sigma_{\rm thin}$ $(\rm km\,s^{-1})$	Reference ID[a]	$V_{\rm mod}$ $(\rm km\,s^{-1})$	σ $(\rm km\,s^{-1})$	$V_{\rm in}$ $(\rm km\,s^{-1})$	$T_{\rm ex}$ (K)	τ	$\bar{\chi}^2$	δ_v	δ_v^*
(1)	(2)	(3)	(4)	(5)	(6)	(7)	(8)	(9)	(10)	(11)	(12)
B16	4.1360(1)	0.1150(1)	R3	4.06(2)	0.13(1)	−0.11(4)	7.1(4)	3.4(8)	1.0	...	...
B15	3.9490(2)	0.1550(2)	R4	4.11(3)	0.14(2)	0.26(3)	6.8(3)	4(1)	0.9	...	...
B30	4.1350(1)	0.1680(1)	R7	4.12(3)	0.36(2)	−0.06(4)	7.8(3)	4.5(8)	1.2	...	...
B20	3.5590(9)	0.210(1)	R21	...	...	...	...	...	...	0.42(7)	...
B5	4.720(5)	0.263(2)	K135	...	...	...	...	...	...	−0.69(8)	...
S50	4.9280(3)	0.1860(3)	R33	5.11(2)	0.29(8)	0.3(2)	7.6(7)	2(2)	1.6	...	...
B3	5.060(7)	0.234(3)	K133	...	...	...	...	...	...	0.32(7)	...
B59	7.3(1)	0.21(4)	K125	7.37(2)	0.23(2)	0.23(4)	11.7(5)	3.2(4)	1.2	−0.5(2)	−0.6(1)
B45	7.040(4)	0.144(2)	K124	...	...	...	...	...	...	−0.41(6)	...
S46	8.190(4)	0.204(2)	K123	8.32(3)	0.36(2)	0.06(4)	8.1(3)	4.1(7)	1.3	−0.87(6)	−1.14(8)
B80	7.794(3)	0.307(4)	R64	7.79(2)	0.68(2)	0.07(4)	14.9(1)	1.6(1)	3.3	...	...
B72	7.84(4)	0.33(4)	...	7.537(9)	0.460(7)	−0.51(2)	19.1(2)	4.3(1)	5.3	0.6(1)	1.0(1)
S39[b]	8.25(3)	0.43(2)	...	8.321(7)	0.398(6)	−0.29(2)	17.4(1)	2.2(1)	1.7	0.50(5)	0.43(4)
S37	7.80(4)	0.46(4)	...	...	...	...	...	...	...	0.16(5)	...
B65	8.4830(3)	0.2080(3)	R72	8.67(2)	0.60(3)	−0.1(1)	10.4(4)	0.8(2)	0.9	0.0(2)	−0.4(3)
S34	7.59(5)	0.61(5)	...	7.748(9)	0.451(8)	0.05(2)	14.8(1)	2.0(1)	1.7	0.32(5)	0.22(3)
S32	7.70(1)	0.70(1)	R76	...	...	...	...	...	...	−0.09(1)	...
B67	8.590(5)	0.225(2)	K104	8.60(2)	0.56(3)	0.18(9)	13.9(6)	1.0(2)	1.4	...	...
B74	8.21(2)	0.37(9)	K101	8.07(1)	0.23(2)	0.26(6)	14.2(4)	2.8(4)	1.6	−0.56(3)	−0.40(2)
B55	7.53(5)	0.42(5)	...	...	...	...	...	...	...	0.18(9)	...
B54[c]	7.57(9)	0.29(9)	...	7.66(3)	0.24(4)	0.2(2)	8.4(8)	2(1)	0.7	−0.2(2)	−0.4(1)
B87[b]	8.150(4)	0.149(2)	K95	8.03(1)	0.19(2)	0.26(5)	10.5(4)	4.1(5)	1.2	−1.11(3)	−0.76(5)
B17	6.05(3)	0.13(3)	...	6.07(2)	0.15(1)	−0.03(2)	8.8(5)	6(1)	1.0	...	...
B34	7.83(1)	0.157(5)	K91	7.81(3)	0.20(2)	−0.08(4)	7.0(4)	6(2)	0.9	0.81(8)	0.9(1)
B28	6.9920(1)	0.1820(1)	R99	7.07(2)	0.230(5)	0.2(2)	9.9(6)	1.6(7)	1.7	...	...
B33	6.78(4)	0.43(4)	...	6.86(2)	0.38(2)	0.05(3)	11.6(3)	2.1(2)	1.1	...	...
B41	6.5700(1)	0.1530(1)	R113	...	...	...	...	...	...	−0.1(1)	...
B48	6.920(8)	0.234(3)	K68	6.99(1)	0.24(1)	−0.03(2)	10.5(3)	4.4(5)	1.2	...	...
B115	8.27(0)	0.17(0)	K23	8.37(1)	0.210(8)	0.03(2)	11.7(3)	2.9(3)	1.5	...	...
B104	9.87(3)	0.31(1)	K16	10.07(2)	0.51(4)	0.4(1)	13.8(7)	1.4(3)	1.7	0.31(7)	0.04(6)
S1	10.240(5)	0.191(2)	K4	10.039(9)	0.154(6)	−0.33(1)	9.8(2)	7.0(8)	1.5	0.32(3)	0.77(3)

Note. — Negative infall velocities ($V_{\rm in} < 0$) imply outward motions. Hyperfine structure in NH_3 allows for very accurate velocity measurements (see Rosolowsky et al. 2008 for details).

[a] Letters of the optically-thin reference ID designating the catalog source – K for N_2H^+ (Kirk et al. 2007b) and R for NH_3 (Rosolowsky et al. 2008) surveys – and the core number in the catalog.
[b] Broad line wings in HCO^+ profiles fit by a Gaussian and removed before modeling with HILL5 (Section 4.2.2).
[c] Low S/N N_2D^+ source (Section 4.2.1).

line of sight, increasing toward the core centers. This model best reproduces the physical parameters of the simulated infalling cores that exhibited double-peaked, asymmetric line profiles. The HILL5 model assumes two layers of gas are moving toward or away from each other at a constant velocity within the core.

We use the IDL MPFIT chi-squared minimization routine (Markwardt 2009) to fit the HILL5 model with five free parameters: the line-of-sight systemic velocity of the core with respect to the local standard of rest ($V_{\rm mod}$), the velocity dispersion of the molecular species (σ), the infall velocity ($V_{\rm in}$), the peak excitation temperature of the core ($T_{\rm ex}$), and the line center optical depth (τ). The HILL5 model was run on all HCO^+ detections. We considered a significant result to be one for which the magnitude of the infall velocity was larger than its uncertainty and we report these in Table 3.

The analytic model is defined for *starless* cores and does not account for features that may be present in protostellar cores such as internal heating and molecular outflows. To reduce systematic errors with cores that exhibit features likely to arise from YSOs, such as

high velocity line wings, we fit broad Gaussians to the emission spectra of three sources to remove these broad features before proceeding with the analytic modelling (noted in Table 3). Because our observations are single pointings, we cannot distinguish between cores with negative infall velocities that are being powered by molecular outflow jets and those that are expanding or are oscillating about an equilibrium (Lada et al. 2003; Lee & Myers 2011a; Broderick & Keto 2010). We argue that protostellar cores, especially those with signatures of high velocity line wings in their emission profiles, are likely to be powered by YSO-driven molecular outflows. Indeed, all three cores from which broad line wings were removed were found to be protostellar. Being able to identify cores with negative infall velocities as being the result of outflows, however, is beyond the scope of this study. We therefore refer to cores with negative infall velocities in general as having "expanding" profiles, but in the case of protostellar cores with high velocity line wings, such emission profiles are also called more specifically "outflow" profiles.
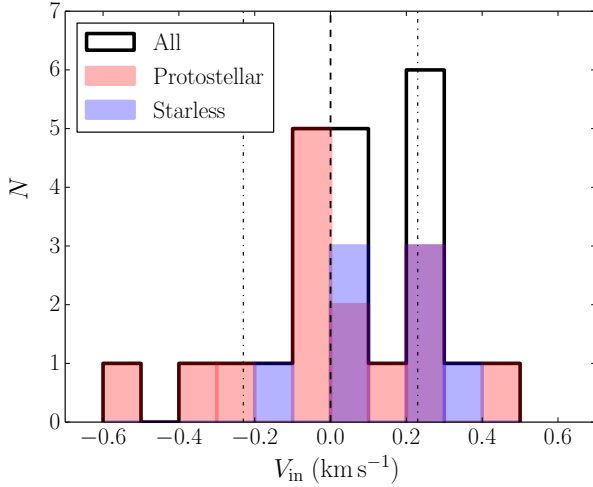
We show an example spectrum where an outflow pro-

Figure 3. Histograms of V_{in} values found for dense cores modeled with the analytic HILL5 model. Note that negative infall velocities ($V_{in} < 0$) imply outward motions. The total distribution is shown in black, with protostellar and starless core distributions shown in red and blue, respectively. Cases where the number of protostars in a bin overlaps the number of starless cores are shown in purple. The vertical dashed line indicates the $V_{in}=0$ line, separating expanding sources (left) from collapsing sources (right). The vertical dotted lines indicate the approximate sound speed of the molecular gas (assuming a gas temperature close to a dust temperature $T_d = 10$ K).

file for source S39 was modeled using the HILL5 model in Figure 2 (right). This source was one of the three whose line wings were removed, and it can be seen that the analytic model does a very good job at fitting the line profile for this source. The analytic model determines $V_{in} < 0$, as one might expect from the strong red asymmetry seen in HCO$^+$. The solid and dashed vertical lines indicate the systemic velocity traced by N$_2$D$^+$ and that provided by the analytic model, respectively; these agree very closely.

The physical parameters provided by the HILL5 model for 23 cores are listed in Columns 5 through 10 of Table 3. The model-derived systemic velocity (V_{mod}) is listed in Column 5, the velocity dispersion (σ) in Column 6, the infall velocity (V_{in}) in Column 7, the optical depth (τ) in Column 9, and the reduced chi-squared goodness of fit parameter ($\bar{\chi}^2$) in Column 10. Note that negative infall velocities ($V_{in} < 0$) imply outward motions. The resulting analytic model fits are shown in Figure A.3 in the Appendix.

Of the 23 cores that reveal significant radial motion when modeled with HILL5, and hence have results listed in Table 3, 14 have $V_{in} > 0$, indicative of infalling or collapsing motions, while the remaining 9 show expanding motions. We find that protostellar sources comprise the majority (15/23, or 65 %) of cores with measured infall or outflow speeds. Similar fractions of starless and protostellar cores show infall motions (7 out of 27 protostellar sources, and 7 out of 31 starless sources detected in HCO$^+$ show infall motions, after removal of sources with multiple cores along the line of sight), while protostellar cores are significantly more likely to show expanding motions (8 out of 27 versus 1 out of 31 for starless cores), likely due to outflows driven by embedded YSOs. Figure 3 shows the distribution of V_{in} for protostellar and

starless cores, in red and blue, respectively, and the entire distribution shown in black. We discuss the range in infall speeds further in the next section, but note that on average, protostellar sources are found to have higher infall speeds than the starless cores. The statistics from the model-derived infall velocity results are summarized in Table 2.

5. DISCUSSION

5.1. Comparison of δ_v and the HILL5 Model

To test the efficacy of using the infall parameter of Mardones et al. (1997) as an indicator of dense cores undergoing collapse in Perseus, we compare directly δ_v and V_{in} in Figure 4 (left). As one might hope, the line asymmetries quantified by δ_v approximately anti-correlate with the infall velocity, V_{in}, found by the model. However, there is a broad scatter between these two infall tracers and there are two sources in the upper-right quadrant where δ_v and V_{in} disagree on the direction of radial motion.

In some cases, the multiple Gaussian fitting routine does not always accurately reproduce the velocity of the brightest component in the optically-thick emission profile. This is more prominent with profiles that have narrow features or shoulders where the velocity components are not well separated. This results in V_{thick} being red-shifted or blueshifted from the velocity of the brightest component and, in some cases, the opposite sign of δ_v than expected. Another source of variation between δ_v and V_{in} occurs when the observed systemic velocity does not perfectly coincide with the line profile center, which can more significantly affect δ_v in cases where the emission line profile shows narrow features or shoulder profiles as mentioned above. We note that without removing sources with known or suspected multiple cores along the line of sight, the correlation is substantially worse, emphasizing the necessity of using the optically-thin V_{LSR} as an additional constraint on infall analyses.

The self-absorption dip in optically-thick emission occurs at the systemic velocity of the core, which should trace the line profile center if the line asymmetry is due to radial motion. To investigate the effect that the subtle systemic velocity offsets from the HCO$^+$ line profile centers have on the correlation between δ_v and V_{in}, we repeat the correlation analysis using a modified infall parameter, δ_v^*. This modified infall parameter replaces the systemic velocity, V_{thin}, with the HILL5 model-derived systemic velocity, V_{mod} (see Equation 1). Figure 4 (right) shows V_{in} versus δ_v^*. The anti-correlation is slightly stronger; δ_v identifies core infall relatively well when the optically-thin systemic velocity accurately traces the line profile center of the optically-thick emission profile (or vice versa), as is explored further in the following discussion.

In Figure 5 (top) we plot the systemic velocity (V_{thin,HCO^+}) of cores with symmetric HCO$^+$ profiles against V_{thin}, showing that the line centers determined for HCO$^+$ and N$_2$D$^+$ agree exceptionally well where both species are optically thin. In Figure 5 (bottom), we show the same correlation between V_{mod}, the systemic velocity provided by the analytic model, and V_{thin}. Figure 6 shows the distribution of residuals between the symmetric HCO$^+$ line profile centers, the model-derived systemic velocity, and the systemic velocity traced by
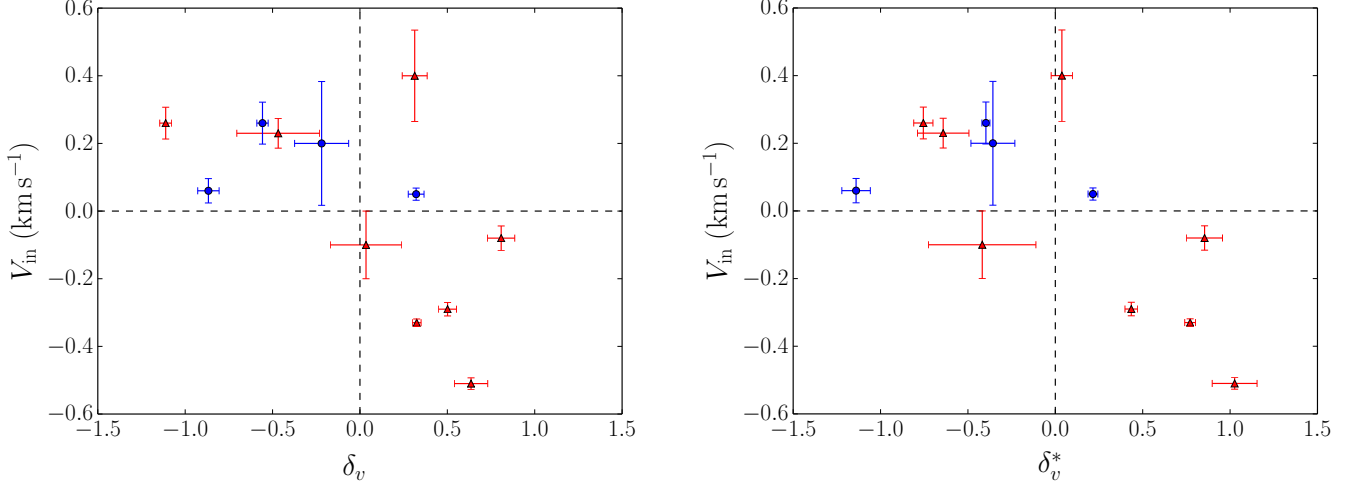
Figure 4. Left: Modeled infall velocities for asymmetric HCO^+ profiles versus the calculated infall parameter, δ_v. Starless cores are indicated with (blue) circles and protostellar cores with (red) triangles. The Pearson correlation coefficient between these two parameters is $\rho_{PCC} = -0.60$. Note that negative infall velocities ($V_{in} < 0$) imply outward motions. Right: Modeled infall velocities for asymmetric HCO^+ profiles versus the modified calculated infall parameter, δ_v^*, which uses the model-derived systemic velocity in replacement of that observed with Nitrogen-based optically-thin tracers. Starless cores are again indicated with (blue) circles and protostellar cores with (red) triangles. The correlation between these two parameters is $\rho_{PCC} = -0.69$.

the optically-thin Nitrogen-bearing molecular tracers. A more stringent test is obtained from the residuals; in both cases the distributions are similar, with median values of $0.01 \, \mathrm{km \, s^{-1}}$ and $0.07 \, \mathrm{km \, s^{-1}}$ for the optically-thin and optically-thick cases, respectively. Figure 6 shows that the line profile centers are well measured by the Nitrogen-bearing molecular tracers in both the optically-thin and optically-thick HCO^+ samples, but that the median values and the dispersions are not insignificant compared to measured infall velocities.

5.2. *Observed Infall Speeds*

In starless cores, infall speeds are often subsonic when measured with molecular lines that trace similar densities to the HCO^+ transition observed here. For example, Lee & Myers (2011b) find typical infall speeds $V_{in} \sim 0.05$ to $0.09 \, \mathrm{km \, s^{-1}}$ in emission from CS (2–1). Similarly to this study, Schnee et al. (2013) use HCO^+ (3–2) to determine $V_{in} \sim 0.1$ to $0.2 \, \mathrm{km \, s^{-1}}$. Both papers target well-studied starless cores within several nearby star-forming clouds (none of which overlap with our survey).

These infall speeds are greater than predicted by ambipolar diffusion contraction models (Ciolek & Mouschovias 1995). In an analytic model of pressure-free collapse of centrally condensed cores, Myers (2005) finds maximum infall speeds of $\sim 0.1 \, \mathrm{km \, s^{-1}}$ at later times in the collapse ($t \sim 0.5 \, t_{ff}$, where t_{ff} is the free-fall time, and $t = 0$ is the start of core collapse), and subsonic maximum infall speeds over most of the collapse timescale. In the inside-out collapse model of Shu (1977), infall velocities $\gtrsim 0.1 \, \mathrm{km \, s^{-1}}$ can be reached over the extent of a core, but only at later times when a protostar has already formed and should be visible at infrared wavelengths. Higher infall speeds at outer core radii are predicted by hydrodynamic collapse models that converge to Larson-Penston flows (e.g., Foster & Chevalier 1993); however, these highly supersonic infall speeds are generally not observed in starless cores.

Where detected, we find infall speeds ranging between small, subsonic values ($0.03 \, \mathrm{km \, s^{-1}}$) to large, supersonic values ($0.4 \, \mathrm{km \, s^{-1}}$) at the typical temperatures of star-forming cores in Perseus ($\sim 11 \, \mathrm{K}$; Rosolowsky et al. 2008). Of the six cores with infall speeds greater than the sound speed at this typical temperature ($c_s = 0.2 \, \mathrm{km \, s^{-1}}$), five are in clustered environments such as NGC 1333 and IC 348. This raises the question of whether, in clustered regions, the infall speeds determined through modeling of the HCO^+ emission are tracing global, rather than local, infall. We also find that a larger percentage of cores in NGC 1333 show substantial line asymmetries relative to cores in less clustered regions in Perseus. Global infall has been identified toward NGC 1333 by Walsh et al. (2006) through HCO^+ (1–0) and HCO^+ (3–2) maps. They found supersonic infall speeds $V_{in} \sim 0.5 \, \mathrm{km \, s^{-1}}$, determined through similar line modeling to that performed here, over much of the NGC 1333 complex rather than being limited to individual cores. High resolution mapping of optically-thick species that trace high densities would help to disentangle the effects of local and global collapse, but we suspect that the transonic infall speeds found in this survey are generally dominated by global collapse motions rather than local infall.

Finally, we note that the sensitivity in this survey might not be high enough to detect large numbers of cores with very low infall speeds. The ability of the HILL5 model to determine the infall speed of an asymmetric line profile accurately is strongly dependent on the S/N of the spectrum, and the model works best when the red and blue peaks are well separated, with an intensity difference between the red peak and self-absorption trough that is at least 10 % of the intensity of the blue-shifted peak. While we detect many of the cores in HCO^+ with S/N > 10, some sources with small infall speeds, lower optical depths in the HCO^+, or subtle line asymmetries would have large uncertainties in V_{in} and so
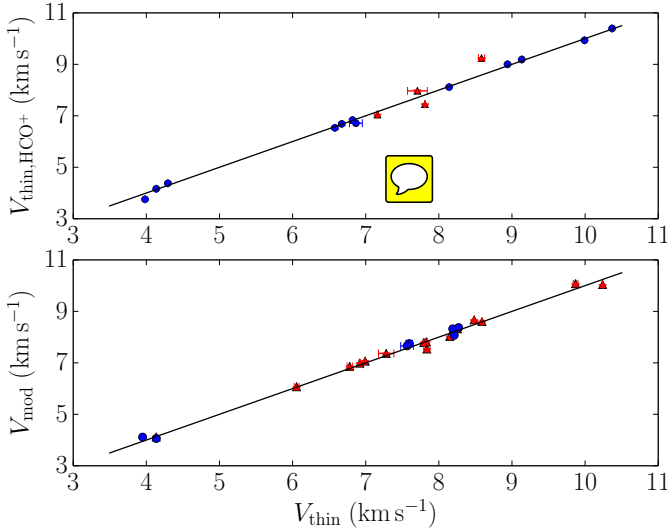
Figure 5. Correlations between the systemic velocity ($V_{\mathrm{thin,HCO^+}}$) of optically-thin HCO$^+$ profiles (top) and model-derived systemic velocities (V_{mod}) of optically-thick HCO$^+$ profiles (bottom), with the systemic velocity obtained from their optically-thin counterparts (V_{thin}). The Pearson correlation coefficient between the two measures is ρ_{PCC}=0.99 for $V_{\mathrm{thin,HCO^+}}$ (top) and ρ_{PCC}=1.00 for V_{mod} (bottom), respectively. Starless cores are indicated with (blue) circles and protostellar cores with (red) triangles. The solid diagonal lines represents the 1:1 correspondence.
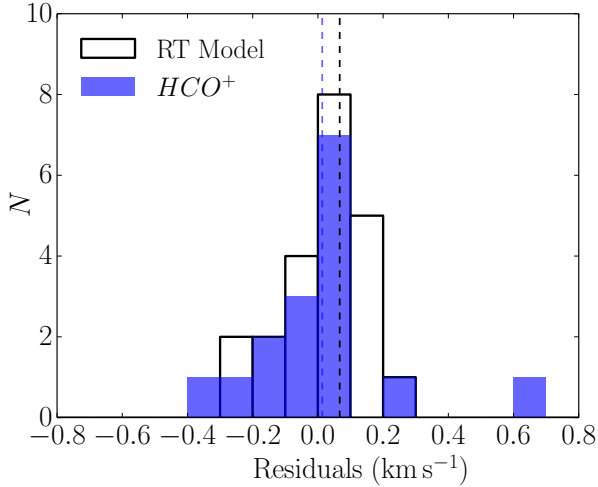
Figure 6. Distributions of residuals between the centroid velocities for the symmetric HCO$^+$ profiles (blue) and the modeled systemic velocity for asymmetric HCO$^+$ profiles (white) and the systemic velocity provided by the Nitrogen-based optically-thin molecular tracers. The vertical dashed lines indicate the median residual value for each distribution, 0.01 km s^{-1} for the $V_{\mathrm{thin,HCO^+}}$ of the symmetric HCO$^+$ profiles (blue) and 0.07 km s^{-1} for the modeled V_{mod} of the asymmetric HCO$^+$ profiles (black). The distribution of residuals for $V_{\mathrm{thin,HCO^+}}$ and V_{mod} have a standard deviation of 0.22 km s^{-1} (approximately the sound speed of the molecular gas) and 0.13 km s^{-1}, respectively.

not be regarded as significant in our analysis.

5.3. Infall and Core Stability

The stability of dense cores requires the counterbalancing of their own self-gravity and any external pressures by their internal means of support. Here we investigate the ratio of the core masses to their Jeans mass (M_{J}), the critical mass that a gas cloud can support (not collapsing under its own self-gravity) assuming only thermal support is important. Higher ratios of core mass to Jeans mass (M/M_{J}) should thus be indicative of cores more likely to exhibit ongoing star formation and $M/M_J = 1$ defines the critical self-gravitating limit. The Jeans mass is expected to be particularly relevant in cold, quiescent dense cores, where the turbulent motions from the surrounding molecular cloud have dissipated substantially. In agreement with this, in a survey of prestellar cores in the Ophiuchus molecular cloud Simpson et al. (2011) show that M/M_{J} is a good predictor of core instability, finding that between 40 % to 60 % of cores with $M/M_{\mathrm{J}} > 1$ show evidence of line asymmetries that they attribute to infall. Similarly, in a sample of highly evolved, starless cores across multiple molecular clouds, Schnee et al. (2013) show that infall motions are more likely in cores with $M/M_{\mathrm{J}} > 1$.

We first determine masses for all cores detected in HCO$^+$, with one exception, using 1.1 mm (Enoch et al. 2006) and 850 μm (Kirk et al. 2006) surveys of Perseus (note that we use the fluxes reported in Kirk et al. 2007a). For each source, we identify the nearest (sub)mm core within 15″ of our targets and calculate the core mass using

$$M = \frac{d^2 F_\nu}{\kappa_\nu B_\nu(T_d)}, \qquad (3)$$

where d is the distance to Perseus, F_ν is the total observed (sub)mm flux density, κ_ν is the dust opacity at frequency ν, and $B_\nu(T_d)$ is the Planck function at dust temperature T_d. We use a dust opacity $\kappa = 0.018\,\mathrm{cm^2\,g^{-1}}$ at 850 μm and $\kappa = 0.0114\,\mathrm{cm^2\,g^{-1}}$ at 1.1 mm, in accordance with the Ossenkopf & Henning (1994) dust models with ice mantles. These two values are consistent with one another for an emissivity spectral index of ~ 2, typical for dense cores. Rosolowsky et al. (2008) determine the gas kinetic temperature, T_{K}, for many of the Perseus cores. We set $T_d = T_{\mathrm{K}}$ where our targets agree within 15″ and set $T_d = 11$ K, the mean T_{K} for all detected cores in Perseus, for cores with no overlap with Rosolowsky et al.. At the densities typical of most of the cores observed here ($n \gtrsim 10^{4.5}\,\mathrm{cm^{-3}}$; Kirk et al. 2006; Enoch et al. 2006), we expect the gas and dust to be coupled (Doty & Neufeld 1997; Goldsmith 2001). This assumption is therefore not a significant source of uncertainty in the final masses. The single starless core with no reported continuum flux density, and hence no calculated core mass, showed no line asymmetry in the detected HCO$^+$ line.

We next determine the Jeans mass for each core following Sadavoy et al. (2010):

$$M_{\mathrm{J}} = 1.9 \left(\frac{T_d}{10\ \mathrm{K}}\right) \left(\frac{R_J}{0.07\ \mathrm{pc}}\right) \mathrm{M_\odot}. \qquad (4)$$

Here, we set $R_{\mathrm{J}} = R_{\mathrm{eff}}$ from the continuum surveys to estimate the Jeans radius. In Table 4 we list the effective core radius (R_{eff}) from the continuum surveys, the derived core mass (M), and the gas kinetic temperature (T_{K}) where measured, as well as the Jeans mass and

Table 4
Continuum Masses and Stability of the Perseus Cores

| Source | Continuum | | Gas | | Jeans Analysis | |
	$R_{\rm eff}$ (pc)	M (M$_\odot$)	$T_{\rm K}$[a] (K)	$\sigma_{\rm H_2}$ (km s^{-1})	$M_{\rm J}$ (M$_\odot$)	$M/M_{\rm J}$
B16	0.06	0.3	9.2	0.09	1.4	0.2
B15	0.05	0.4	9.2	0.14	1.3	0.3
B31	0.11	0.9	10.0	0.12	3.1	0.3
B11	0.13	2.8	10.3	0.11	3.7	0.7
B30	0.04	3.1	12.1	0.15	1.3	2.4
S57	0.04	3.1	11.2	0.14	1.4	2.3
B27	0.10	1.7	11.2	0.18	2.9	0.6
B24	0.04	4.5	9.1	0.13	1.1	4.0
B23	0.06	1.2	9.0	0.14	1.5	0.8
B20	0.09	0.7	· · ·	· · ·	2.7	0.3
B5	0.06	0.6	13.1	0.26	2.1	0.3
S50	0.03	1.3	10.5	0.17	0.8	1.6
B2	0.04	1.8	11.4	0.15	1.1	1.6
B3	0.04	1.6	11.9	0.20	1.2	1.3
B43	0.09	1.1	10.6	0.13	2.6	0.4
B59	0.03	1.5	12.4	0.20	1.1	1.3
B45	0.06	0.6	10.5	0.13	1.9	0.3
S46	0.04	2.2	11.7	0.17	1.3	1.7
S44	0.04	1.9	11.7	0.18	1.2	1.7
B64	0.06	0.4	11.3	0.10	1.7	0.2
B80	0.05	2.8	14.4	0.30	1.8	1.5
B56	0.01	0.2	12.5	0.19	0.5	0.4
B72	0.05	4.8	16.4	0.25	2.4	2.0
S39	0.04	5.8	16.3	0.28	1.9	3.0
B71	0.07	1.0	13.6	0.23	2.7	0.4
S37	0.04	2.2	14.8	0.35	1.5	1.5
S35	0.04	3.3	· · ·	· · ·	1.3	2.5
B65	0.08	2.2	12.6	0.19	2.6	0.8
S34	0.04	3.8	· · ·	· · ·	1.2	3.1
S32	0.04	3.0	· · ·	· · ·	1.2	2.5
B67	0.05	4.0	14.3	0.21	1.9	2.1
B74	0.03	0.4	15.5	0.41	1.1	0.4
B55	0.06	1.2	· · ·	· · ·	1.8	0.7
B54	0.06	0.7	· · ·	· · ·	1.9	0.4
B87	0.02	0.9	10.5	0.10	0.7	1.2
B17	0.09	1.9	10.0	0.13	2.4	0.8
B34	0.10	1.5	10.5	0.13	3.0	0.5
B28	0.05	1.4	11.4	0.17	1.7	0.9
B33	0.04	7.2	11.7	0.23	1.2	5.8
B37	0.12	4.5	10.2	0.11	3.4	1.3
B38	0.11	2.2	11.2	0.22	3.3	0.7
B40	0.09	2.2	10.1	0.12	2.3	0.9
B41	0.07	0.9	10.0	0.14	1.8	0.5
B42	0.07	0.9	9.9	0.18	1.8	0.5
B44	0.07	0.9	9.7	0.10	1.8	0.5
B48	0.08	0.8	11.9	0.24	2.5	0.3
B77	0.08	0.8	· · ·	· · ·	2.3	0.3
B112	0.04	2.5	11.7	0.18	1.4	1.8
B115	0.03	1.1	12.9	0.16	1.2	0.9
B106	0.06	0.8	13.0	0.26	2.3	0.3
B102	0.08	0.8	11.0	0.21	2.3	0.3
B100	0.11	1.6	10.5	0.14	3.2	0.5
B104	0.05	0.6	16.0	0.33	2.1	0.3
B103	0.07	0.8	10.8	0.10	2.0	0.4
B116	0.13	2.7	10.7	0.08	3.7	0.7
S2	0.03	1.4	10.1	0.17	0.9	1.6
S1	0.03	1.0	11.7	0.15	0.9	1.2

[a] For cores with no overlap with Rosolowsky et al. (2008), we set $T_d = 11$ K, the mean $T_{\rm K}$ for all detected cores in Perseus.

ratio of core mass to Jeans mass, $M/M_{\rm J}$.

Our sample has an average core mass of 1.9 M$_\odot$ and an average $R_{\rm eff}$ of 0.06 pc. The protostellar cores have, on average, larger masses and smaller effective radii than the starless cores. Over all the Perseus cores with HCO$^+$ detections, we find an average $M_{\rm J} = 1.9$ M$_\odot$. The starless core population has a greater average Jeans mass than the protostellar cores (2.0 M$_\odot$ versus 1.7 M$_\odot$, re-

spectively). Just over half of the protostellar cores have $M/M_{\rm J} > 1$ (16 of 27), compared with only 24 % (7 of 30) of starless cores (see Table 2; note that one starless core does not have an associated core mass). These seven supercritical starless cores are interesting candidates for future studies on evolving dense cores.

Figure 7 (left) shows $M/M_{\rm J}$ as a function of $V_{\rm in}$ for the Perseus cores. The horizontal dashed line at $M/M_{\rm J} = 1$ shows the transition between sub-critical and super-critical thermally-supported cores. In the figure proto-stellar and starless cores are identified separately (red tri-angles and black circles, respectively). Cores that were found not to show infall or outflow motions above our threshold in the HILL5 model fitting are assigned an in-fall velocity of zero, with no error bars, and are also sepa-rated into protostellar and starless populations. The fig-ure shows that we find inward and outward motions over the entire range of core $M/M_{\rm J}$ ratios, and in addition many cores with $M/M_{\rm J} > 1$ without substantial inward or outward motions. We note, however, that a larger fraction of protostellar cores with $M/M_{\rm J} > 1$ (9 of 16) show infall or outflow motions when compared with sub-critical protostellar cores showing infall or outflow mo-tions (6 of 11). In the protostellar case, core masses are continuously lowered as material accretes onto the cen-tral star, possibly reducing the core mass to Jeans mass ratio for more evolved (but still deeply embedded) pro-tostellar cores.

Most starless cores do not show evidence for inward or outward motions (22 of 31 cores). The fraction of starless cores having a measured infall velocity is larger for the supercritical case $M/M_{\rm J} > 1$ (3 of 7) compared to the subcritical case (4 of 23). The overall fraction of supercritical starless cores showing infall motions is thus similar to that found in Ophiuchus (43 % vs. 40-60 %; Simpson et al. 2011), although Perseus does not have a large number of supercritical starless cores. No supercrit-ical starless cores have measured outward motions, while for the subcritical case there is one, along with the four with inward motion, a similar finding to Schnee et al. (2013). In starless cores, outward motions have been at-tributed to oscillations of the core around an equilibrium (Lada et al. 2003; Lee & Myers 2011a; Broderick & Keto 2010) or to core expansion. Without spectral line maps of this one core, however, we cannot distinguish between these scenarios.

In summary, overall we find seven of 31 HCO$^+$-detected starless cores that show evidence for infall, or 23 % of the starless core sample, while over half of protostellar cores have infall or outflow motions traced by HCO$^+$. Thermally supercritical cores are somewhat more likely to show infall motions compared to subcriti-cal cores. Most starless cores in Perseus are likely not in a state of collapse (or expansion). Kirk et al. (2007b) find that many cores in Perseus that overlap with our sam-ple are consistent with being in virial equilibrium if the external pressure from the ambient cloud is taken into account. In their analysis, the authors model the cores as Bonnor-Ebert (BE) spheres to determine the external pressure. For a critical BE sphere, $M_{\rm BE} = 2 M_{\rm J}$.

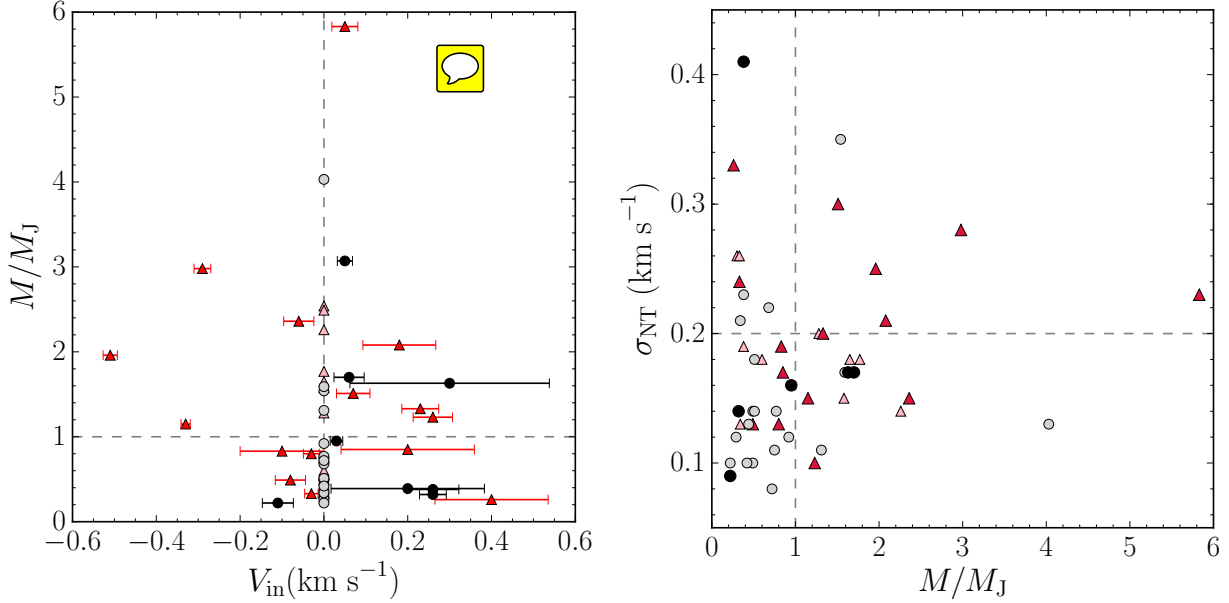### 5.4. Non-Thermal Motions Traced by Optically-thin Line Widths

Figure 7. Left: Scatterplot of the core mass as a fraction of the Jeans mass versus the modeled infall velocity (V_{in}). Note that negative infall velocities ($V_{in} < 0$) imply outward motions. Cores with no detected infall or outflow motions have been assigned $V_{in} = 0$. Right: Scatterplot of the non-thermal line width as measured by optically-thin emission lines versus the core mass as a fraction of Jeans mass. Horizontal line indicates the sound speed for H_2 at 11 K. In both plots, circles indicate starless cores; black circles indicate starless cores with measured radial (infall or outflow) motions and grey circles indicate "static" starless cores. Triangles indicate protostellar cores; red triangles indicate protostellar cores with measured radial (infall or outflow) motions and light red triangles indicate static protostellar cores.

While optically-thin lines do not show the asymmetric line profile indicative of infall seen in optically-thick emission, any global infall motion will result in observed line profiles that are wider than in cores that are not undergoing collapse or expansion (Myers 2005), given similar thermal and non-thermal, non-infall motions. Undetected infall or outflow motions in classified "static" cores might therefore result in a trend of increased line widths at larger M/M_J ratios. To explore this, we determined the non-thermal velocity dispersion, σ_{NT}, for all HCO$^+$-detected sources with optically-thin line detections in this paper, Rosolowsky et al. (2008), or Kirk et al. (2007b), using

$$\sigma_{NT} = \sqrt{\sigma_{thin}^2 - \frac{k_B T_K}{A m_H}}. \tag{5}$$

where A is the mass number of the molecular species. As before, we set T_K based on NH$_3$-derived gas temperatures and assume $T_K = 11$ K for those sources without gas temperatures measured through NH$_3$ observations. The non-thermal velocity dispersion is listed for each core in Table 4.

On average, cores with measured infall/outflow motions have greater σ_{NT} than static cores, but there is no clear trend between σ_{NT} and V_{in}. We show in Figure 7 (right) σ_{NT} as a function of M/M_J, separating the cores into those with detected infall or outflow motions and static cores. Protostellar cores with measured infall or outflow motions tend to have greater σ_{NT} with increasing M/M_J, but there are exceptions. No trend is seen, however, for starless or protostellar cores without measured infall or outflow motions. Below the critical value $M/M_J = 1$, both starless and protostellar cores have σ_{NT} values that range from subsonic to transonic (the sound

speed for H_2 at 11 K is $c_s = 0.2\,\mathrm{km\,s^{-1}}$), although a larger fraction show subsonic σ_{NT}. Above $M/M_J = 1$, all static starless and protostellar cores, as well as starless collapsing cores, have subsonic σ_{NT}, with one exception.

Since we find no trend in σ_{NT} with M/M_J for the static cores, we conclude that any undetected infall motions are small and subsonic. In the centrally-condensed, pressure-free collapse model of Myers, optically-thin line widths remain narrow at early times ($t \lesssim 0.3 t_{ff}$), while collapse timescales are longer for the more realistic isothermal case by a factor ~ 1.6. This suggests that, as noted above, most of the starless cores in Perseus are either not currently in a state of collapse, or are in the very early stages where infall speeds are low.

6. SUMMARY

We have performed a pointed molecular line survey of 91 dense starless and protostellar cores in Perseus. Observations of HCO$^+$ and N$_2$D$^+$ rotational transitions were made using the James Clerk Maxwell Telescope, detecting 72 cores in HCO$^+$ and 24 in N$_2$D$^+$.

1. We identify line asymmetries in optically-thick HCO$^+$ line profiles using a dimensionless infall parameter, δ_v (Mardones et al. 1997). We quantify line asymmetries for 20 of the cores and find that protostellar cores are more likely to exhibit line asymmetries than are starless cores.

2. We fit all HCO$^+$ line profiles with an analytic infall model (De Vries & Myers 2005), and determine the physical infall velocity toward 23 Perseus cores with asymmetric line profiles that are well-fit by the model. We find only 7 of 31 starless cores (where we detect HCO$^+$ and find no evidence of

multiple components along the line-of-sight) have spectra indicative of infall motions and classify the remaining cores as "static." Over half of protostellar cores show infall or outflow motions, and protostellar cores are far more likely than starless cores to show expanding motions, likely the result of outflows caused by embedded YSOs. Given a mean dust temperature $T_d = 11$ K for Perseus, we find 6 sources that have infall speeds greater than the sound speed of the molecular gas, significantly larger than previously observed infall velocities toward starless cores. Of these sources 5 reside in clustered environments such as NGC 1333, suggesting that toward these cores the HCO^+ emission is tracing global rather than local collapse motions.

3. We investigate the relationship between the dimensionless infall parameter (δ_v) and the model-derived infall velocity (V_{in}) and find that δ_v is a good indicator of core infall if the model-derived systemic velocity accurately traces the line profile center, *when sources where multiple cores are likely overlapping along the line of sight are removed.* When using δ_v as a tracer of infall, obtaining accurate V_{thin} measurements is critical for identifying these overlapping sources, particularly in clustered regions.

4. We determine the ratio of core mass to Jeans mass (M_J). We find no overall trend between V_{in} and M/M_J, but show that for both starless and protostellar sources, supercritical cores (where $M/M_J > 1$) are more likely to have infall or outflow motions.

5. In general, protostellar cores with known infall or outflow motions also show increasing non-thermal line widths with M/M_J. This is not true for cores where we do not identify infall or outflow-related line asymmetries. Furthermore, below $M/M_J = 1$, static cores have both transonic and subsonic non-thermal line widths, while all static cores (with one exception) with $M/M_J > 1$ have subsonic non-thermal line widths. This indicates that any undetected infall or outflow motions are likely small and subsonic. Most starless cores in Perseus are therefore either not collapsing (or expanding), or are in the very early stages of collapse.

The ability to study the complete kinematics of the Perseus cores is limited by the fact that these observations consist of single pointings. If the cores are evolving as described by the inside-out collapse model (Shu 1977), then cores in the earliest stages of collapse might not experience infall across the entire extent of the core and might go undetected if our pointing is off-center. Future studies involving spectral line maps would be useful to test whether most Perseus cores are not in a state of collapse (or expansion), or if many are in the earliest stages of collapse that have gone undetected. Line maps would also help to disentangle the effects of local (core) and global collapse, as well as better identify molecular outflow in sources with negative infall velocities.

REFERENCES

Adelson, L. M., & Leung, C. M. 1988, MNRAS, 235, 349 1
Aikawa, Y., Ohashi, N., & Herbst, E. 2003, ApJ, 593, 906 1
Bergin, E. A., & Tafalla, M. 2007, ARA&A, 45, 339 1
Broderick, A. E., & Keto, E. 2010, ApJ, 721, 493 4.2.2, 5.3
Cernicharo, J. 1991, in NATO ASIC Proc. 342: The Physics of Star Formation and Early Stellar Evolution, ed. C. J. Lada & N. D. Kylafis, 287 1, 1
Cernis, K. 1993, Baltic Astronomy, 2, 214 1
Chen, X., Arce, H. G., Zhang, Q., et al. 2010, ApJ, 715, 1344 2, 2
Chira, R.-A., Smith, R. J., Klessen, R. S., Stutz, A. M., & Shetty, R. 2014, ArXiv e-prints, arXiv:1402.5279 1
Ciolek, G. E., & Mouschovias, T. C. 1995, ApJ, 454, 194 5.2
De Vries, C. H., & Myers, P. C. 2005, ApJ, 620, 800 1, 4, 4.2.1, 4.2.2, 2
Doty, S. D., & Neufeld, D. A. 1997, ApJ, 489, 122 5.3
Emprechtinger, M., Caselli, P., Volgenau, N. H., Stutzki, J., & Wiedner, M. C. 2009, A&A, 493, 89 4.2.1
Enoch, M. L., Evans, II, N. J., Sargent, A. I., & Glenn, J. 2009, ApJ, 692, 973 1, 2, 2
Enoch, M. L., Young, K. E., Glenn, J., et al. 2006, ApJ, 638, 293 1, 1, 2, 5.3, 5.3
Evans, N. J., Dunham, M. M., Jorgensen, J. K., et al. 2009, VizieR Online Data Catalog, 218, 10321 1
Foster, P. N., & Chevalier, R. A. 1993, ApJ, 416, 303 5.2
Friesen, R. K., Kirk, H. M., & Shirley, Y. L. 2013, ApJ, 765, 59 2
Gerin, M., Pearson, J. C., Roueff, E., Falgarone, E., & Phillips, T. G. 2001, ApJ, 551, L193 4.1
Goldsmith, P. F. 2001, ApJ, 557, 736 5.3
Gregersen, E. M., Evans, II, N. J., Mardones, D., & Myers, P. C. 2000, ApJ, 533, 440 1
Jijina, J., Myers, P. C., & Adams, F. C. 1999, ApJS, 125, 161 2
Jørgensen, J. K., Johnstone, D., Kirk, H., & Myers, P. C. 2007, ApJ, 656, 293 1, 2, 2
Kirk, H., Johnstone, D., & Di Francesco, J. 2006, ApJ, 646, 1009 2, 5.3, 5.3
—. 2007a, ApJ, 669, 657 5.3
Kirk, H., Johnstone, D., & Tafalla, M. 2007b, ApJ, 668, 1042 1, 4, 4.2.1, 3, 5.3, 5.4
Lada, C. J., Bergin, E. A., Alves, J. F., & Huard, T. L. 2003, ApJ, 586, 286 4.2.2, 5.3
Lada, E. A., Strom, K. M., & Myers, P. C. 1993, in Protostars and Planets III, ed. E. H. Levy & J. I. Lunine, 245–277 1
Ladd, E. F., Lada, E. A., & Myers, P. C. 1993, ApJ, 410, 168 1
Ladd, E. F., Myers, P. C., & Goodman, A. A. 1994, ApJ, 433, 117 1
Larson, R. B. 1969, MNRAS, 145, 271 1
Lee, C. W., & Myers, P. C. 2011a, ApJ, 734, 60 4.2.2, 5.3
—. 2011b, ApJ, 734, 60 5.2
Leung, C. M., & Brown, R. L. 1977, ApJ, 214, L73 1, 4.2.1
Luhman, K. L., Stauffer, J. R., Muench, A. A., et al. 2003, ApJ, 593, 1093 1
Mardones, D., Myers, P. C., Tafalla, M., et al. 1997, ApJ, 489, 719 1, 1, 4.2.1, 4.2.1, 5.1, 1

Markwardt, C. B. 2009, in Astronomical Society of the Pacific
    Conference Series, Vol. 411, Astronomical Data Analysis
    Software and Systems XVIII, ed. D. A. Bohlender, D. Durand,
    & P. Dowler, 251 4.2.2
Myers, P. C. 1985, in Protostars and Planets II, ed. D. C. Black
    & M. S. Matthews, 81–103 1
Myers, P. C. 2005, ApJ, 623, 280 5.2, 5.4, 5.4
Myers, P. C., Bachiller, R., Caselli, P., et al. 1995, ApJ, 449, L65
    4.2.1
Myers, P. C., Evans, II, N. J., & Ohashi, N. 2000, Protostars and
    Planets IV, 217 1
Narayanan, G., Moriarty-Schieven, G., Walker, C. K., & Butner,
    H. M. 2002, ApJ, 565, 319 1
Ossenkopf, V., & Henning, T. 1994, A&A, 291, 943 5.3
Rosolowsky, E. W., Pineda, J. E., Foster, J. B., et al. 2008, ApJS,
    175, 509 2, 4, 4.2.1, 3, 5.2, 5.3, 4, 5.4
Sadavoy, S. I., Di Francesco, J., & Johnstone, D. 2010, ApJ, 718,
    L32 5.3

Schlafly, E. F., Green, G., Finkbeiner, D. P., et al. 2014, ApJ,
    786, 29 1
Schnee, S., Brunetti, N., Di Francesco, J., et al. 2013, ApJ, 777,
    121 5.2, 5.3, 5.3
Schnee, S., Francesco, J. D., Enoch, M., et al. 2012, ApJ, 745, 18
    2, 2
Shu, F. H. 1977, ApJ, 214, 488 1, 5.2, 6
Simpson, R. J., Johnstone, D., Nutter, D., Ward-Thompson, D.,
    & Whitworth, A. P. 2011, MNRAS, 417, 216 5.3, 5.3
Snell, R. L., & Loren, R. B. 1977, ApJ, 211, 122 1
Snell, R. L., Loren, R. B., & Plambeck, R. L. 1980, ApJ, 239, L17
    1
Černis, K. 1990, in Nordic-Baltic Astronomy Meeting, ed. C.-I.
    Lagerkvist, D. Kiselman, & M. Lindgren, 75–78 1
Walsh, A. J., Bourke, T. L., & Myers, P. C. 2006, ApJ, 637, 860
    5.2
Zhou, S. 1992, ApJ, 394, 204 1

APPENDIX

Observed line profiles for all 72 detections of HCO^+ are shown in Figure A.1, with sources in order of increasing RA as in Table 1. Profiles for 23 detections of N_2D^+ are shown in Figure A.2, along with the profile for B54 where the N_2D^+ line has S/N of only 2.3 but is well aligned with that of its HCO^+ counterpart.

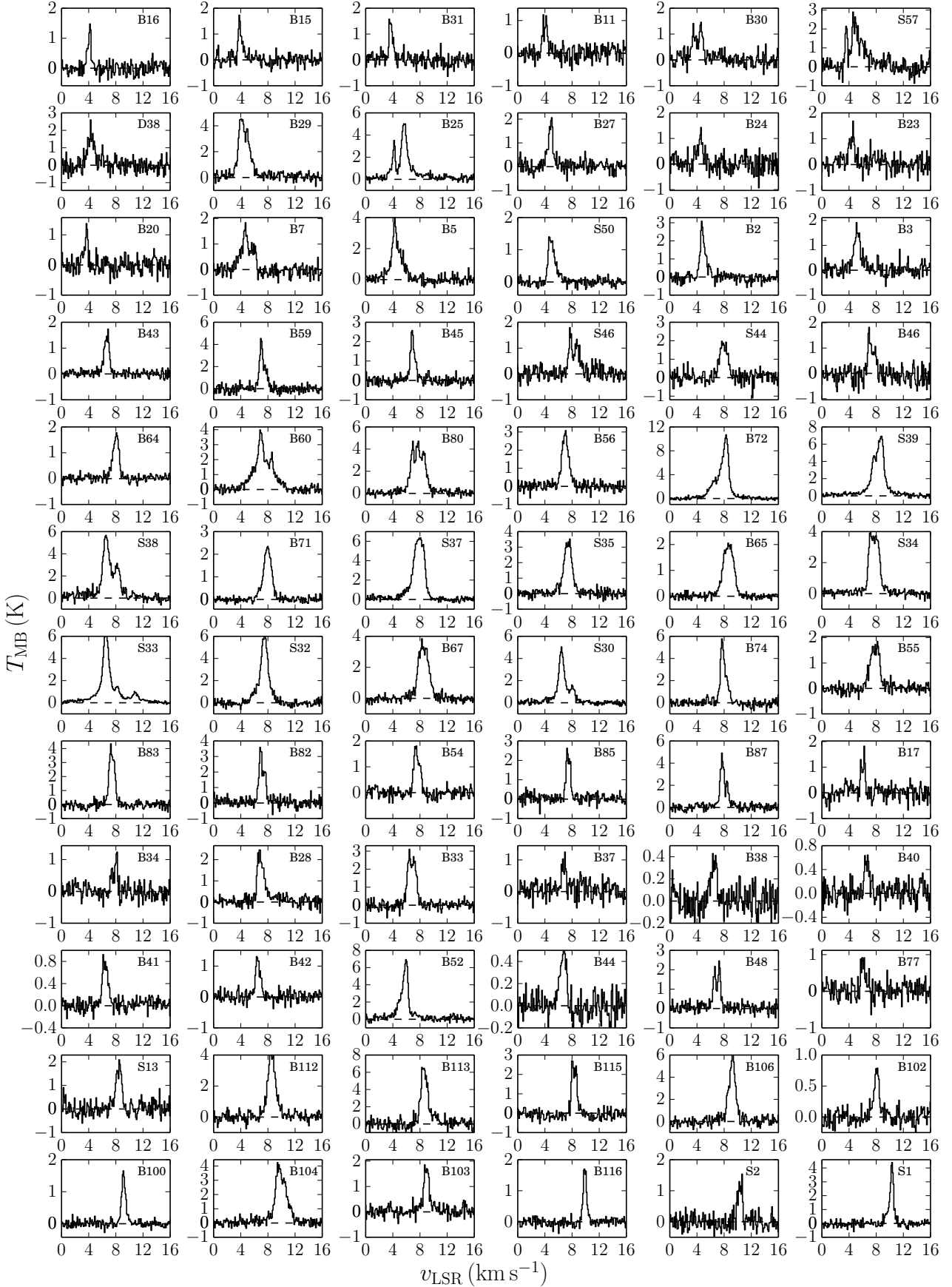Figure A.3 shows the analytic fits to the 23 HCO^+ line profiles analysed with the HILL5 model.

Figure A.1. Line profiles for 72 HCO$^+$ detections. The velocity scale is identical in all plots but the temperature scale differs.
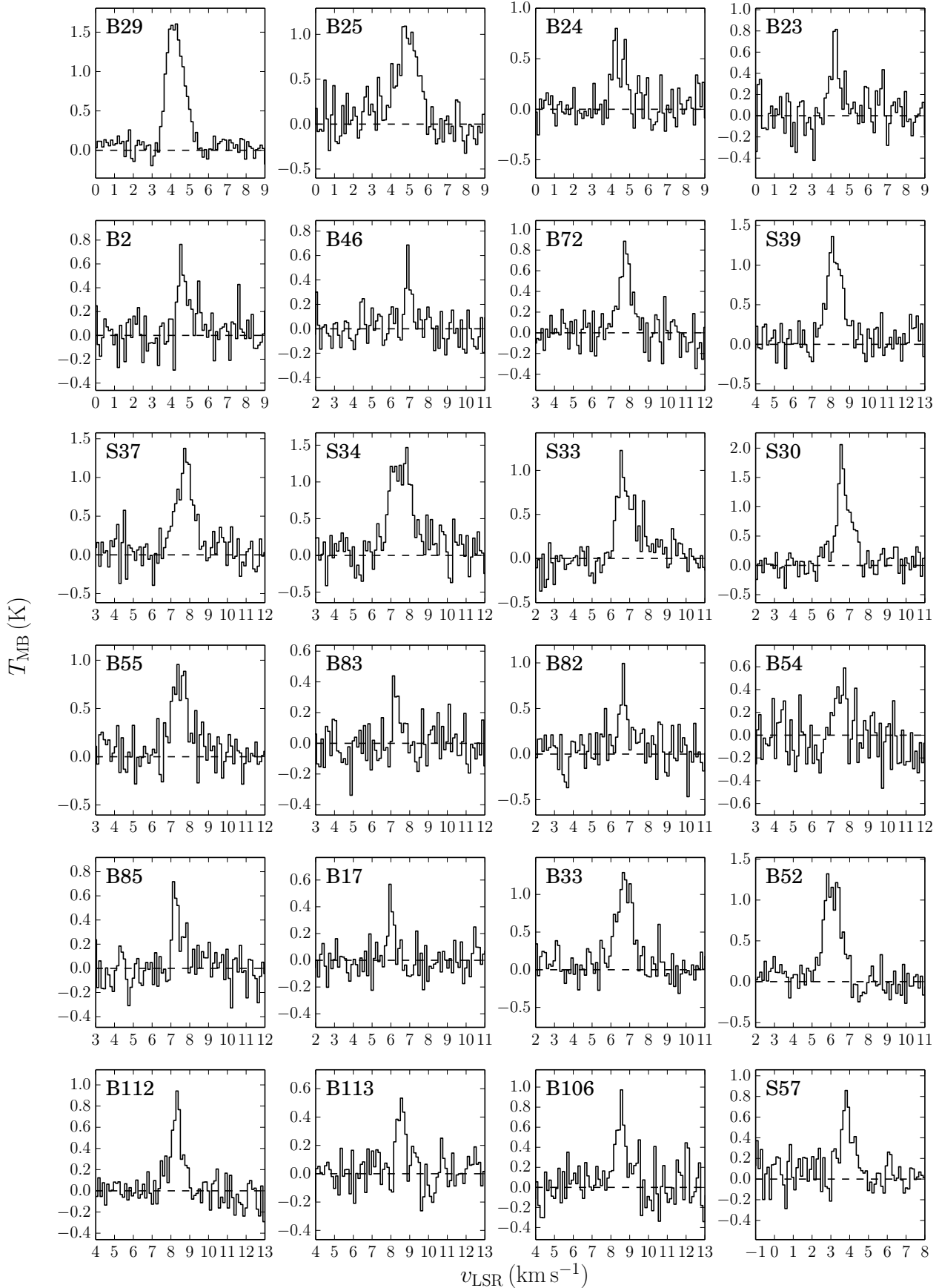
Figure A.2. Line profiles for 23 N_2D^+ detections and one low S/N detection (B54, discussed in Section 3). The velocity range is identical in all plots but the temperature scale differs.
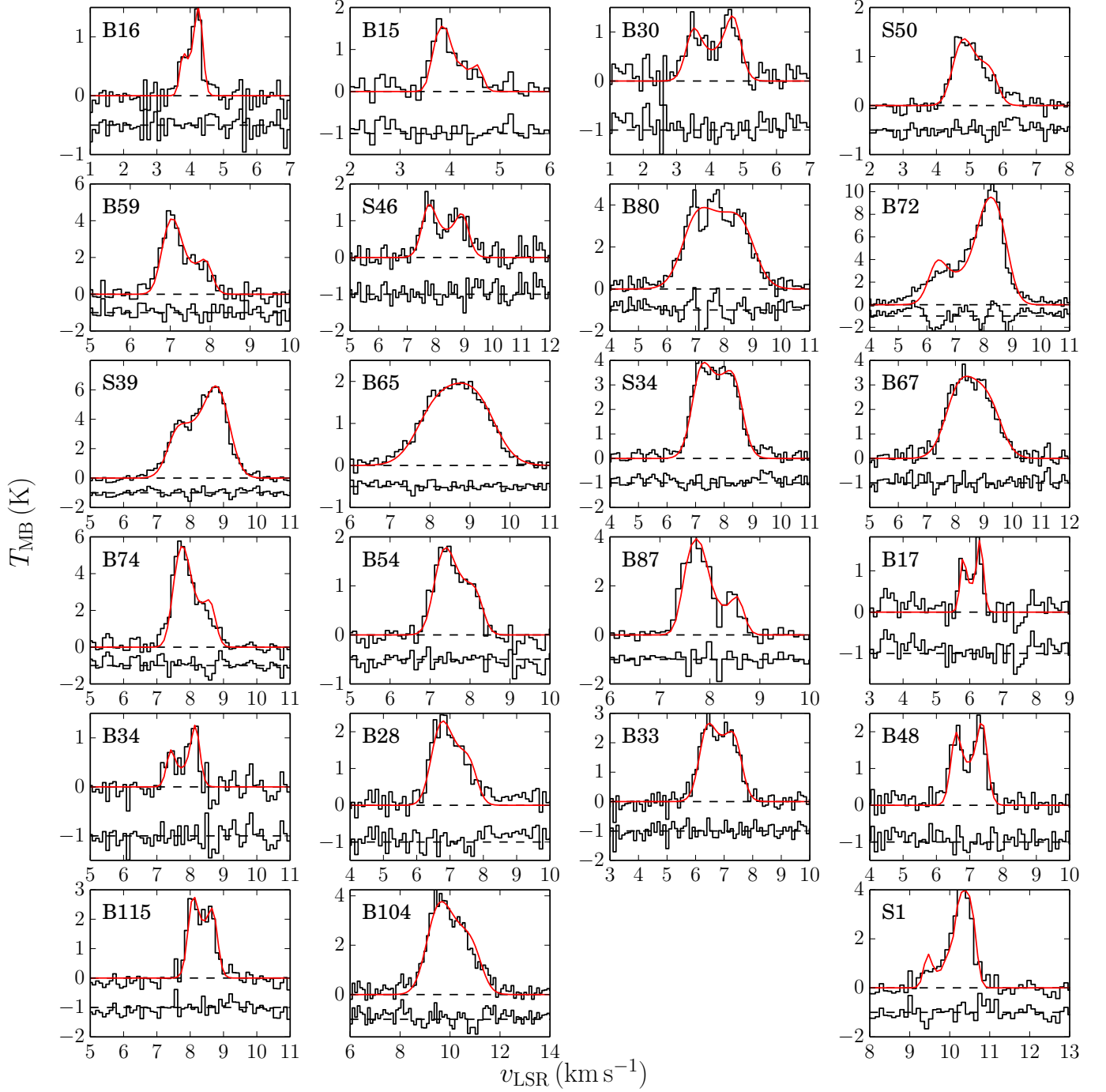
Figure A.3. Line profiles for 23 cores whose HCO$^+$ emission was modeled with the analytic HILL5 model. The HCO$^+$ profile is shown along the 0 K baseline with the analytic model best fit over-plotted (red). The resulting residuals are plotted below, displaced to centre on −1 K.